# Experimental observations that simulated active-layer deepening drives deeper rock fracture

Article (Accepted Version)

**Experimental observations that simulated active-layer deepening drives deeper rock fracture**

Vikram Maji[1] and Julian B. Murton[2]

Permafrost Laboratory, Department of Geography, University of Sussex, Brighton BN1 9QJ, UK

[1] Corresponding author; v.maji@sussex.ac.uk; [2] j.b.murton@sussex.ac.uk

## Abstract

The impact of changes in active-layer thickness on the depth of pervasive macrofracture (brecciation) in frost-susceptible bedrock is unclear but important to understanding its physical properties and geohazard potential. Here we report results from a laboratory experiment to test the hypothesis that active-layer deepening drives an increase in the depth of brecciation. The experiment simulated active-layer deepening in 300 mm cubic blocks of limestone (chalk) and sandstone. Temperature, surface heave and strain at depth were measured during 16 freeze–thaw cycles. Macrocracks photographed at intervals were digitally analysed to visualise crack growth and to quantify crack inclination and length. In chalk, an upper horizon of macrocracks developed first at about 100 mm depth in a shallow thaw active layer during cycles 1–8, followed by a lower horizon at about 175–225 mm depth in a deeper thaw active layer during cycles 9–16. The longest cracks (>35 mm) were most common at inclinations of 0–30° from horizontal, and numerous cracks <5 to 15 mm long developed at inclinations of 40–50°, with some longer vertical to subvertical cracks linking the two brecciated horizons. Overall, the observations support the hypothesis that a thickening active layer drives deeper rock fracture by ice segregation.

Keywords: Active layer, freeze–thaw, ice segregation, limestone, rock fracture, sandstone, strain

## 1. Introduction

Rock fracture by freeze–thaw is an important geomorphic process in periglacial regions.[1] The initiation and development of fracture networks, however, remain to be investigated in detail. Little is known about (1) the impact of changes in active-layer thickness (ALT) on the depth of pervasive macrofracture (brecciation), (2) the magnitude and location on strain at depth within rock prior to and during fracture, (3) the propagation of microfractures and transition into macrofractures, and (4) the timing and location of microfracture events during freeze–thaw cycles. To elucidate these issues we carried out a laboratory experiment[2] to monitor the strain and fracture of two types of sedimentary rock and report the observations in two companion papers. The present paper addresses issues (1) and (2), and the second paper addresses issues (3) and (4).

Active-layer deepening and permafrost warming have characterised many polar and alpine regions in recent decades.[3] Laboratory experiments have shown that warming permafrost is likely to warm and weaken ice that fills joints in rock by lowering the factor of safety,[4] thus increasing the risk of slope instability. What is less clear is the impact of active-layer deepening on the formation of new, deeper fractures, which may further weaken bedrock and deepen the engineering rockhead (the rock surface at the base of an engineering soil). Some insight into this was provided by laboratory experiments and numerical simulations that demonstrated that the freezing regime (uni- or bidirectional freezing) determines the depth of fracture of frost-susceptible limestone,[5] but the model remains to be tested against an experimentally deepened active layer. We hypothesize that active-layer deepening drives an increase in the depth of brecciation by ice segregation in frost-susceptible bedrock.

Here we describe the experimental set-up and report observations of temperature, simulated ALT, strain and macrofracture with the aim of testing this hypothesis. The main objective is to

determine the relationship between the base of the simulated active layer and macrofracture by visualizing the development of a growing network of cracks using digital image analysis of time-series photographs. A subsidiary objective is to examine how the orientation of primary stratification in rock influences its thermal conditions and deformation.

# 2. Material and Methods

## 2.1 Rock types and specimen preparation

Two rock types were tested, a soft, frost-susceptible, homogeneous chalk and a harder, non-frost-susceptible, inhomogeneous sandstone. The chalk is Saint Cyr Tuffeau, a siliceous chalk of Turonian (Upper Cretaceous) age and was collected from Lucet Quarry, Brézé-Saint-Cyren-Bourg, 10 km south of Saumur, France. The chalk contains small fragments of fossils but is otherwise relatively homogeneous and shows freezing behaviour similar to frost-susceptible silty–clay.[5] The sandstone is fine to medium-grained, poorly cemented and well laminated, from one of the two Masonry 'lifts' (beds) of the Ardingly Sandstone Member of the Tunbridge Wells Sand Formation.[7] It is of Valanginian (Lower Cretaceous) age and was collected from Philpots Quarry, West Hoathly, West Sussex, UK. The sandstone has a greater density and compressive strength (2130 kg $m^{-3}$ and 72 MPa) than the chalk (1350 kg $m^{-3}$ and 0.53–9.24 MPa), but a lower porosity (23–27% in sandstone and 47% in chalk).[8–9] Both rock types have been used in previous laboratory experiments.[10–11] Two blocks of sandstone and one of chalk were cut at the quarries. The block dimensions (300 mm cubes) were sufficient for macroscale fractures to develop at a size almost comparable to those at field scale. [5, 12] The blocks were air dried in the laboratory prior to installation in the cold room.

## 2.2 Freezing system and cold-room layout

The freezing system in the cold room of the Permafrost Laboratory at the University of Sussex

has a chilled air fan for downward cooling of samples, and a basal cooling plate for upward freezing. The cooling plate (manufactured by Freezertech, Humberston, UK) is tabular, with dimensions of 1500 x 600 x 50 mm, and chilled by gas circulating inside. The plate is thermostatically controlled, to maintain a maximum and user-controlled freezing temperature in the lower part of blocks. To simulate thawing periods (summers), the chilled-air fan was turned off and the door of the cold room opened, allowing warm air to enter the cold room and initiate downward thawing of the simulated active layer from the top surface of the blocks. An aluminium tank 1895 mm long, 750 mm wide and 500 mm high was installed within the cold room to contain the rock blocks and cooling plate. A polystyrene sheet 25 mm thick was placed on the bottom of the tank (to insulate it from the base of the tank) and the cooling plate was placed directly upon the sheet.

Position for figure 1

Position for figure 2

The three blocks were placed inside the tank and wetted prior to freezing (Figures 1 and 2). The four corners at the base of each block were placed on an acetyl pillar (40 mm diameter, 10 mm thick) resting on the top of the cooling plate. The resulting 10 mm air gap beneath each block was later filled with water, and the water table set about 10 mm above base of the blocks, to allow them to wet by capillary rise (Figure 3). For one sandstone block the lamination was oriented horizontally (SH) and for the other it was oriented vertically (SV), to investigate how the orientation influences the rate of capillary rise, strain and fracture. The blocks were left for several days to wet through, as indicated by the capillary front reaching the top of the blocks. Polystyrene insulation was placed around the vertical faces of the blocks to minimise lateral heat transfer and set up a vertical temperature gradient during freeze–thaw cycles, to simulate bidirectional freezing of a horizontal active layer in bedrock.

Position for figure 3

Initially, the blocks froze from the top down, controlled by the chilled-air system. During downward freezing, water was free to drain out of the bottom of the tank. When the temperature at the bottom of the blocks reached –10°C, the cooling plate beneath them was turned on to maintain subzero temperatures in the lower part of the blocks thereafter, in order to simulate permafrost. Sixteen freeze–thaw cycles—each comprising a freezing period (air temperatures ranged between $0^0$C and -$15^0$C) and a thawing period (air temperatures ranged between $0^0$C and $30^0$C )—were carried out over a duration of 465 days. During freezing periods the chilled air temperature was maintained according to temperature set in the basal cooling plate for different phases, while during thawing periods the chilled air supply system was turned off and air at ambient room temperature was allowed to enter in the cold room and thaw the upper part of the blocks. The cycles are grouped into four phases that represent three temperature protocols for the permafrost, as determined by the thermostatically-controlled basal cooling plate. The plate thermostat was set to –15°C for phase one (P1: cycles 1–4, days 0–68), –10°C for P2 (cycles 5–8, days 69–203), and –5°C for both P3 (cycles 9–12, days 207–312) and P4 (cycles 13–16, days 315–465).

## 2.3 Temperature

The temperature of the rock was measured with platinum resistance thermometers manufactured by British Rototherm Co Ltd. The resistors are 100Ω at 0°C (Pt100) and consist of a PR2825 element made to BS EN60751:1996 Standard, 4 wire, Class A (see ref. 12 for details). The Pt100s were calibrated in an ice–water bath (0°C). In each block, five Pt100s were installed within holes 6 mm in diameter and 45 mm long drilled along the central vertical axis of face D, spaced 50 mm apart (Figure 2) from depths of 50 to 250 mm to monitor the vertical thermal profile. Gaps between the Pt100s and the sides of the holes were filled with a mixture of rock dust (produced

during drilling of the blocks) and gypsum (2:3 ratio) to ensure a good contact between the sensors and the rocks.[14] A dilute solution of gypsum ($CaSO_4$, $2H_2O$) was used to bond the sensor firmly to the rock. The maximum depth of penetration of the 0°C isotherm was determined from time series of temperature profiles to estimate the maximum depth of the thaw front during each thawing period (to simulate the base of the active layer during summer).

## 2.4 Heave and settlement of the block top

Heave and settlement of the block tops were measured by linear variable differential transformers (LVDTs) model LDC 1000C (with captive guided armature), manufactured by RDP Group. According to the manufacturer, their linearity is ±0.35% of the full range, and their sensitivity exceeds 46 mV $mm^{-1}$. Each LVDT was calibrated individually using different metal slips of known thickness. A black acetyl rod (8 mm diameter) of variable length was screwed on to each LVDT leg such that the voltage value reaches the most sensitive state in response to any small vertical displacement (near the centre of the core). The foot of the rod rested on the middle of the top face of each block (Figure 3).

## 2.5 Strain at depths within the blocks

Strain at different depths on the surface of the vertical faces of the blocks was measured by miniature strain gauges. The changes in resistance within the gauge were measured using a Wheatstone bridge configuration, with an excitation voltage (direct current) supply. The configuration has four arms, each with a resistance. Eight strain gauges were mounted on the vertical faces of the chalk block—five aligned vertically on face B and one on faces A, C and D—and four gauges were aligned vertically on face B of both sandstone blocks (Figures 1 and 2). The strain gauges had 120 Ω resistor values (RS Pro wire lead strain gauge, part No. 632-124), with a gauge factor of two (which measures the sensitivity of the gauge). The gauges were mounted on the face

of test specimen using epoxy—X-60 (methylmetacrylate) two-component adhesive manufactured by HBM, such that strain retained within the deformed body was transferred into the gauges. Before mounting the gauges, an area of rock was smoothed with sandpaper to ensure a good contact between the gauge and the rock.

The temperature effect on the resistance of the strain gauge wires was minimised using two dummy strain gauges replacing the resistance arm on the Wheatstone bridge configuration. Any changes in temperature affect both gauges equally such that the ratio of the resistors remains the same and the effect of temperature change is minimised. Dummy gauges were mounted with the same epoxy on three plastic rulers 300 mm long, in the same order and depth as the gauges on the rock surfaces. Two metal screws were inserted through the top and bottom of each ruler into the block to mount the dummy gauges adjacent to their counterpart gauge mounted on the rock. The top screw was inserted through an elongate slit (3 mm wide, 25 mm long) through the ruler, allowing the block to move independently of the ruler along the measurement plane of the gauges.

The two-arm Wheatstone bridge circuit with 100 times gain (16-signal conditioning electrical circuit) was encased within a thermally insulated box inside the cold-room to minimise the temperature-dependent resistance associated with long wire cables. Prior to the experiment, the 16-signal conditioning electrical circuit was calibrated in both extension and compression regimes to obtain a similar gain value. The error range was then further minimised, repeating the test in different temperature regimes to simulate the freeze–thaw cycles and establish a calibration curve for each signal conditioning circuit. The temperature ranges used to calibrate the circuits are within the limits of the temperature window used in the experiment.

Data on temperature, heave and strain were logged a National Instruments CompactDAQ multiplexed USB data acquisition system (model NI cDAQ-9172) connected to four 32-channel analog input modules (model 9205). The measurement and control system used LabVIEW software.

Mean values of data sampled at rates of 2.5 kHz over 10-minute intervals were recorded into a text (.txt) file format. The LabVIEW virtual interface was programmed to generate a single text file of all the data recorded at 24-hr intervals.

### 2.6 Image analysis

Vertical face B of the three blocks was photographed at intervals during the experiment in order to image the rock surface condition and reveal any macrocracks. Face B was selected as it was the only accessible face in the experimental tank without disturbing the experimental set up. At the end of the experiment (after freeze–thaw cycle 16) all four vertical faces of the blocks were photographed. Well-exposed portions of photographs of face B of the fractured chalk block after cycles 8, 12 and 16 were digitally analysed to record progressive macrocrack development. The macrofracture phase was isolated from the material phase following the Otsu (1979)[15] method of thresholding. Based on the connectivity within the crack network, the fracture phase was classified into multiple clusters and each cluster highlighted with a different colour. Best-fit ellipses covering each of the individual clusters of fracture networks were fitted around the visible fractures using *ImageJ* software (U.S. National Institutes of Health, USA). The length and inclination of the ellipses that represent the fracture clusters were also quantified using *ImageJ* software.

## 3. Results

### 3.1 Capillary rise

The rate of capillary rise was fastest in the sandstone block with vertical lamination (SV: 6 hours to wet through), and slowest in the chalk block (17–18 hours). The sandstone block with horizontal lamination (SH) had an intermediate rate of capillary rise (12 hours). Photographs of the rising capillary fronts are shown in Figure 3.

## 3.2 Air temperature

The mean air temperature (± 1 std dev) during freezing (F) periods varied between about −12 ± 0.83 °C in cycle 3 (F3) to 2 ± 1.42 °C in F13, and that during thawing (T) periods varied between about 7 ± 1.95 °C in cycle 4 (T4) and 25 ± 6.04 °C in T16 (Figure 4a). The temperature was lowest in F2 to F5, and tended to increase in later cycles. The median air temperature during thawing periods increased monotonically between T4 and T18.

Position for figure 4a

## 3.3 Rock temperature

The rock temperature, both in the simulated permafrost and the active layer, generally increased during the course of the experiment (Figure 4b–d). For all three blocks, freezing periods 2–5 were the coldest (–15 to –10°C), as shown by the widespread dark blue colours in the left-hand side of Figure 4b–d. Rock temperature during thawing periods tended to increase from phases 1 (cycles 1–4) to 4 (cycles 13–16), indicated by the deepening location of the 0°C isotherm. The highest temperature recorded (about 10–15°C; during simulated thaw seasons was measured in the upper several tens of millimetres of the chalk during thawing periods of phases 3 and 4 (cycles 9–16). Note that the high temperature and low temperature recorded throughout all the blocks between days 203 and 207 (i.e. between phases 2 and 3), and between days 312 and 315 (between phases 3 and 4) represent pauses in the experimental simulation.

Position for figure 4b–d

## 3.4 Simulated active-layer thickness (ALT)

The simulated ALT in all three blocks generally increased through time (Figure 5). The simulated ALT was least during cycles 2–4 (0 to about 148 mm), intermediate during cycles 5–8 (about 36–210

mm), and greatest during cycles 11–16 (about 162–282 mm). During the particularly cold thermal protocol of phase 1 (basal cooling plate thermostat set to −15°C), a simulated active layer did not develop in the sandstone with vertical lamination (SV) in freezing periods 3 and 4, nor in sandstone horizontal (SH) in freezing period 4. Chalk had a thicker thaw layer than both sandstone blocks during cycles 1–12 (phases 1–3), whereas SH had a thaw layer thicker than that in chalk or SV in cycles 13–16 (phase 4). SV consistently had the thinnest thaw layer of the three blocks, except in cycle 13. Mean values of simulated ALT (± 1 std dev) during phases 1–4 were 112.5 ± 42.8, 173 ± 23.9, 251.8 ± 31.2 and 235.3 ± 15.8 mm, respectively, in chalk, 64 ± 68.4, 156.8 ± 33.3, 159.3 ± 46.6 mm and 246.3 ± 23.5 mm in SH, and 30.8 ± 55.7, 54.3 ± 17.1, 144.8 ± 32.2 and 214 ± 40.8 mm in SV.

Position for figure 5

### 3.5 Heave and settlement of the block tops

Heave and settlement of the block tops varied according to rock and temperature conditions, as shown in the four phases of the experiment (Figure 6). During phase 1, when the rock temperature was lowest (Figure 4b–d), both sandstone blocks heaved substantially during thawing periods 3 and 4, with SH heaving about 4 and 1 mm, respectively, and SV heaving about 1.5 and 1 mm (Figure 6a). By contrast, the chalk heaved only about 0.2 and 0.7 mm. During the thawing periods, the temperature gradient between the top and bottom of each block was relatively high (compared to that during the freezing periods) and fairly stable through time (Figure 6b).

Position for figure 6

During phase 2, all blocks settled substantially during day 87 (early part of thawing period 5), before heave of about 0.2–0.8 mm recommenced at day 92 (later part of thawing period 5). From thawing period 6 onwards, the chalk tended to heave and settle more than both sandstone blocks. The chalk heaved about 5 and 4 mm during thawing periods 6 and 7, respectively, settled about 5.5

mm during the early part of thawing period 8 before heaving about 6.7 mm during the middle and later parts of this period.

Phase 3 began with substantial settlement of all three blocks on day 203, as the blocks completely thawed. Subsequently during phases 3 and 4, the chalk heaved substantially in thawing periods 11 and 14 to 16, with a net overall heave of about 11 mm relative to the start of the experiment. Also, blocks SH and SV show minor progressive heave of about 0.1–0.2 mm during thawing periods, from cycle 9 onwards.

### 3.6 Strain at depth within the blocks

Strain (ε) in the middle to upper horizons of the chalk block typically exceeded that in the lower horizon (Figures 7a and 8a). The chalk showed microstrain (με, i.e., ε x $10^{-6}$) changes of 300–400 in P1 and P2 during the transitions between the freezing and thawing periods, though changes of about 1000–1500 occurred at 150 mm depth (Figure 7a). Microstrain of about 100–200 occurred during each freezing period of P1 and P2 when the temperature gradients were negligible (0°C $mm^{-1}$) and stable. Microstrain at 150 mm depth in face B during thawing periods ranged between about 200 and 600, exceeding that in freezing periods (about 200–400). Overall, the contoured values of microstrain plotted in Figure 8a show that the middle of face B (100–200 mm depth) during P1 and P2 experienced the greatest values of positive microstrain (dilation, shown by orange and red colours) during thawing periods and the greatest values of negative microstrain (contraction: blue colours) during freezing periods. The strain gauge mounted on face A of the chalk recorded error values, and so the data were excluded from analysis.

Position for figure 7

The sandstone horizontal (SH) block showed greater microstrain in the middle horizon of face B than in the upper and lower horizons (Figures 7b and 8b). Microstrain of about 1000–1500 occurred

at 120 and 180 mm during transitions between freezing and thawing periods in P1 and P2, compared with microstrain of about 200–400 at 60 and 240 mm. The microstrain at 60 mm depth exceeded that at 240 mm by about 200 from day 20, with this difference gradually reducing during the remainder of P1 and P2. Unlike those in the chalk block, the contoured values of microstrain between depths of 100 and 200 mm in SH showed contraction (blue colours in Figure 8b) during thawing periods 1 to 7 and the early part of thawing period 8, and dilation (green to yellowish green colours in Figure 8b) during the freezing periods. An error developed in the National Instruments input module collecting the strain data after phase 2, and so strain data are not plotted for phases 3 and 4 for both rock types.

Position for figure 8

## 3.7 Macrocracks

### 3.7.1 Photographs

As freeze–thaw cycling progressed, macrocracks initiated and propagated extensively in the chalk and locally in the sandstone with horizontal lamination (SH) (Figures 9 and 10). In chalk, two macrocrack networks with prominent horizontal to subhorizontal cracks separating discrete lens-shaped rock fragments formed brecciated layers connected by vertical to steeply dipping cracks (Figure 9). By the end of cycle 8, the first network had formed at about 100 mm depth (Figure 9a). In addition, a faint horizontal–subhorizontal macrocrack was visible at about 50 mm depth, and a faint macrocrack had developed on the top surface (not shown), consistent with the development of a vertical or steeply dipping crack inside the chalk. After cycle 12, the second macrocrack network had begun to form at about 175–225 mm depth, while the first network continued to develop (Figure 9b). The crack at about 50 mm depth had become clearer, more extensive and now

connected with the vertical to steeply inclined crack formed near the top of the block (obstructed behind the ruler in Figure 9b). A second steeply inclined crack had developed and connected with the first network at about 100 mm depth. After cycle 16, the macrocrack network at about 175–225 mm depth had grown substantially and a prominent subvertical crack on the left side of the block connected both networks together (Figures 9c and 10b).

Position for figure 9

In block SH, a horizontal macrocrack system was observed at a depth of about 135–145 mm in faces B and C after cycle 16 (Figure 10e and f). The system comprised a number of discrete cracks, some with free ends offset from and overlapping with the free ends of other cracks.

Position for figure 10.1

Position for figure 10.2

### 3.7.2 Digital images

Digital images were produced for the right-hand side of the fracture network at about 100 mm depth in face B of the chalk block after 8, 12 and 16 cycles (Figure 11), and the left-hand side of the network at about 175–225 mm after cycles 12 and 16 (Figure 12), as these areas of the photographs were not obstructed by sensors (Figure 9). In each figure, the panels on the left show individual fracture networks in a separate colour, and the panels on the right show the best-fit ellipses around each cluster. After cycles 8 and 12, small clusters had formed (shown by groups of ellipses in Figure 11b and 11d), connecting the fracture network. After cycle 16, the clusters were more prominent (as indicated by fewer but well-developed ellipses in Figure 11f) and the networks were well developed. Growth of a prominent subvertical crack, as well as horizontal crack propagation, between cycles 12 and 16 is shown in Figure 12.

Position for figure 11

Position for figure 12

Histograms of the length and inclination of macrofractures digitally analysed from the chalk block show that the longest fractures tended to be horizontal to subhorizontal (Figure 13). In both the upper network (about 100 mm depth) and the lower network (about 175–225 mm depth), the longest fractures (>35 mm) were most common at inclinations of 0–30° from horizontal, as shown in light green colours at 0–30° and 150–180°in Figure 13. Additionally, numerous short and medium-length fractures (<5, 5–10 and 10–15 mm long) and a few long fractures (>25 mm) developed at inclinations of 40–50°. The number of short (<5 mm) fractures increased severalfold in the lower network between the end of cycles 12 and 16 (Figure 13d–e).

Position for figure 13.1

Position for figure 13.1

# 4. Discussion

## 4.1 Active-layer deepening and brecciation

The observations of the macrofracture networks produced during this experiment in chalk support the hypothesis that active-layer deepening drives an increase in the depth of brecciation in frost-susceptible bedrock. The deepening of the simulated active layer in the chalk block between phases 1 and 4 (Figure 5) developed at the same time as macrofracture networks initiated and propagated first at a depth of about 100 mm (during P1 and P2) and later at a depth of about 175–225 mm (during P3 and P4) (Figures 9–13). These observations are also consistent with numerical simulations of previous laboratory experiments on the same rock type,[5] and imply that rock fracture was driven by ice segregation focussed near the permafrost table.

The broader implication of the present study is that active-layer thickening or thinning is likely

to generate pervasive macrofracture (brecciation) in the upper metres of frost-susceptible bedrock. This may account for widespread brecciated bedrock observed in regions of past permafrost such as Germany and the UK, in rock types that include fine-grained limestones, fine sandstones, mudrocks and slates[16–17] and of ice-rich brecciated shales, limestones and sandstones in areas of modern permafrost.[18–19] Furthermore, continued climate warming and active-layer deepening in regions of modern permafrost is likely to generate new macrofracture networks, weakening bedrock and increasing risk to some infrastructure.

## 4.2 Macrocrack geometry and propagation

The time series observations of macrocracks elucidate how and where such cracks initiate and propagate. The simple crack system observed at a depth of 135–145 mm in the sandstone horizontal block after 16 freeze–thaw cycles showed a number of discrete cracks with free ends offset from and overlapping each other (Figure 10e–f). Such *interacting* cracks indicate that (1) crack propagation was in opposite directions at each overlap and (2) cracks initiate at many points along a crack system. Similar interacting cracks can also form by thermal contraction cracking of frozen ground above ice wedges.[20]

Vertical to steeply inclined cracks, though less common than horizontal to subhorizontal ones, clearly contribute to crack propagation and brecciation. As such cracks grow (Figure 12a–d) they join horizontal cracks and may connect horizontal crack networks together (Figures 9c and 10b). In fact, all the vertical to steep cracks observed in the chalk block were connected with brecciated layers. The physical significance of such cracks is unclear, though one hypothesis that merits testing in the future is that vertical or steeply inclined cracks represent preferential channels of water movement towards ice lenses relative to water moving through the partially frozen pore network between the cracks. This hypothesis arises from experimental laboratory studies in which vertical

cracks formed *within* the frozen fringe during freezing of silt–clay soils[21–22] or during freezing of colloidal suspensions.[23–25] Such cracks have been described as 'freezing-induced cracks',[26] though it remains to be determined if the tensional stress results from thermal contraction, desiccation or a combination of them. However, caution is needed in comparing cracks formed during freeze- thaw cycling in bedrock (i.e., a cohesive material) with cracks formed in soil, which are related to the suction that develops in the frozen fringe. Thus further research is needed on rock fracture in the frozen fringe.

### 4.3 Rock properties, temperature, heave and strain

The role of rock properties on freezing behaviour and macrocracking is shown by the contrasting observations from the three blocks. The chalk is the softest rock and fractured quickly and extensively within 16 freeze–thaw cycles (Figure 10a–d), whereas the sandstone is harder and fractured slowly and locally, with the first simple crack system not observed until after cycle 16 (Figure 10e–f). This crack system was confined to the sandstone with horizontal lamination (SH) and may reflect the local influence of geological structure aligned more or less parallel to isotherms on the location of ice segregation, in the same way that stratification in soil and sediment can influence the location of ice lenses. [27–30] We speculate that minor variations in texture or local weakness in the crystalline structure between horizontal–subhorizontal laminae focussed ice segregation along them.

The sandstone with lamination vertically oriented (SV) was not observed to crack during the experiment but did freeze more rapidly and to generally lower temperatures than the same rock type with lamination horizontally oriented (Figure 4). SV also wetted by capillary rise faster than SV (Figure 3). Thus, the orientation of the lamination results in anisotropic thermal conductivity and permeability, with vertical lamination enhancing both properties in terms of vertical heat and water

flow. Such findings are significant to studies of mountain rockwalls in which the same lithologies have their stratification oriented differently beneath slopes of varying aspect or gradient, because the thermal and hydrological behaviour of same rock types may vary locally.

The novel experimental method of strain estimation at depth in the rock blocks under dynamic thermal boundary conditions was partially successful. Both rock types (chalk and SH) showed the greatest changes in microstrain at depths of between about 100 and 200 mm during cycles 1–8 (Figure 8), that is, in the central parts of the blocks. For the chalk, it is clear from the heave curve (Figure 6a) that the first macrocrack developed during thawing period 6 (note the heave of about 5 mm then). Thus, the positive microstrains (dilation) recorded in the central horizon of the chalk block during the first 8 cycles probably resulted from progressive microcracking and dilation of this part of the block. What is less certain is why the microstrains for the central horizons of the chalk and SH blocks showed opposite behaviour during cycles 1–8. One possibility is that the dilation of the sandstone during freezing periods reflects volumetric expansion of pore water freezing, in contrast to opening of microcracks and ice segregation in the chalk. But further development and testing of the strain monitoring protocol is needed in future to test this hypothesis.

## 5. Conclusions

The aim of the study was to test the hypothesis that active- layer deepening drives an increase in the depth of brecciation in rock. The hypothesis was tested in a laboratory experiment using one 300 mm cubic block of limestone (chalk) and two blocks of sandstone. The upper part of each block was subject to16 freeze- thaw cycles, while the lower part was maintained at subzero temperature simulating a deepening active layer above permafrost. The following conclusions were drawn from analysis of the experimental observations:

(1) Imaging of macrocracks initiating and propagating in a block of chalk supports the

hypothesis that active-layer deepening drives an increase in the depth of brecciation in frost-susceptible bedrock.

(2) The brecciated horizons consist of discrete lens-shaped fragments rather than continuous fractures.

(3) Vertical to steeply dipping macrocracks observed in chalk were connected with brecciated layers, indicating that such cracks contribute to the development of brecciation, though their cause and function remain to be determined.

(4) Chalk cracked faster and more extensively than sandstone under the same thermal protocol, indicating its relatively high frost-susceptibility.

(5) Miniature strain gauges recorded positive microstrains (dilation) during thawing periods in chalk, consistent with dilation due to ice segregation and micro- and macrocracking.

## Acknowledgements

This research is part of the senior author's doctoral research at the University of Sussex. The research was funded by a Chancellor's international research scholarship and a Global Studies studentship in the Department of Geography. Tim Cane provided valuable help and guidance with experimental design, sample preparation and use of equipment in the Permafrost Laboratory. Comments from Drs P. Cleall and J. Barlow on an earlier version of the manuscript and from two anonymous referees on the present manuscript are appreciated.

## References

1. Ballantyne CK. *Periglacial Geomorphology*. Chichester, UK: Wiley; 2018.

2. Maji V. *An Experimental Investigation of Micro- and Macrocracking Mechanisms in Rocks by Freeze–thaw Cycling*. [PhD thesis]. Brighton: University of Sussex; 2018.

http://sro.sussex.ac.uk/79661/

3. Vaughan DG, Comiso JC, Allison I, et al. Observations: Cryosphere. In: Stocker TF, Qin D, Plattner GK, et al. eds. *Climate Change 2013: The Physical Science Basis. Contribution of Working Group I to the Fifth Assessment Report of the Intergovernmental Panel on Climate Change*. Cambridge, UK and New York, NY, USA: Cambridge University Press; 2013:317–382.

4. Davies M, Hamza O, Harris C. The effect of rise in mean annual temperature on the stability of rock slopes containing ice-filled discontinuities. *Permafrost Periglac.* 2001;12(1):137–144.

5. Murton JB, Peterson R, Ozouf JC. Bedrock fracture by ice segregation in cold regions. *Science.* 2006;314:1127–1129. DOI: 10.1126/science.1132127

6. Murton JB. 2018. Frost weathering of chalk. In: Lawrence JA, Preene M, Lawrence UL, Buckley R. eds. *Engineering in Chalk: Proceedings of the Chalk 2018 Conference, 17–18 September 2018, Imperial College, London*. London, UK: ICE Publishing; 2018:497–502.

7. Radley JD, Allen P. The Wealden (non-marine Lower Cretaceous) of the Weald Sub-basin, southern England. *Proc Geol Assoc.* 2012;123(2):245–318. https://doi.org/10.1016/j.pgeola.2012.01.003

8. Williams RBG, Robinson DA. Weathering of sandstone by the combined action of frost and salt. *Earth Surf Proc Land.* 1981;6(1):1–9. https://doi.org/10.1002/esp.3290060102

9. Murton JB, Coutard JP, Lautridou JP, Ozouf JC, Robinson DA, Williams RBG, Guillemet G, Simmons P. Experimental design for a pilot study on bedrock weathering near the permafrost table. *Earth Surf Proc Land.* 2000;25(12):1281–1294. https://doi.org/10.1002/1096-9837(200011)25:12<1281::AID-ESP137>3.0.CO;2-U

10. Williams RBG, Robinson DA. Experimental frost weathering of sandstone by various combinations of salts. *Earth Surf Proc Land.* 2001(8);26:811–818.

https://doi.org/10.1002/esp.227

11. Murton JB, Ozouf J-C, Peterson R. Heave, settlement and fracture of chalk during temperature cycling above and below 0°C. *Geomorphology.* 2016;270:71–87. https://doi.org/10.1016/j.geomorph.2016.07.016

12. Murton JB, Coutard J-P, Ozouf J-C, Lautridou J-P, Robinson DA, Williams RBG. Physical modelling of bedrock brecciation by ice segregation in permafrost. *Permafrost Periglac.* 2001;12(3):255–266. https://doi.org/10.1002/ppp.390

13. Murton JB, Kuras O, Krautblatter M, Cane T, Tschofen D, Uhlemann S, Schober S, Watson P. Monitoring rock freezing and thawing by novel geoelectrical and acoustic techniques. *J Geophys Res–Earth.* 2016;121(12);2309–2332. doi:10.1002/2016JF003948

14. ASTM Standard C842. *Standard Specification for Application of Interior Gypsum Plaster*. West Conshohocken, PA: ASTM International; 2015.

15. Otsu N. A threshold selection method from grey-level histograms. *IEEE T Syst Man Cyb.* 1979; 9(1):62–66.

16. Büdel J. *Climatic Geomorphology*. Princeton, New Jersey, USA: Princeton University Press; 1982.

17. Murton JB, Ballantyne CK. 2017. Periglacial and permafrost ground models for Great Britain. In: Griffiths JS, Martin CJ, eds. *Engineering Geology and Geomorphology of Glaciated and Periglaciated Terrains – Engineering Group Working Party Report*. London, UK: Geological Society, London, Engineering Group Spec Publ. 28; 501–597. https://doi.org/10.1144/EGSP28.5

18. French HM, Bennett L, Hayley DW. Ground ice conditions near Rea Point and on Sabine Peninsula, eastern Melville Island. *Can J Earth Sci.* 1986;23(9):1389–1400.

19. Hodgson DA, Nixon FM. Ground ice volumes determined from shallow cores from western Fosheim Peninsula, Ellesmere Island, Northwest Territories. 1998. Geol Surv Canada, Bull. 507.

20. Mackay JR. 1993. The sound and speed of ice-wedge cracking, Arctic Canada. *Can J Earth Sci.*

30(3);509–518.

21. Arenson LU, Azmatch TF, Sego DC, Biggar KW. 2008. A new hypothesis on ice lens formation in frost-susceptible soils. In: Kane DL, Hinkel KM, eds. *Proceedings of the 9th International Permafrost Conference, 29 June–3 July, University of Alaska Fairbanks.* Vol. 1. Fairbanks, Alaska, USA: Institute of Northern Engineering, University of Alaska: 2008:59–64.

22. Azmatch TF, Arenson LU, Sego DC. Measuring ice lens growth and development of soil strains during frost penetration using particle image velocimetry (GeoPIV). In: Kane DL, Hinkel KM, eds. *Proceedings of the 9th International Permafrost Conference, 29 June–3 July, University of Alaska Fairbanks.* Vol. 1. Fairbanks, Alaska, USA: Institute of Northern Engineering, University of Alaska: 2008:89–93.

23. Peppin SSL, Worster MG, Wettlaufer JS. Morphological instability in freezing colloidal suspensions. *Proc R Soc A.* 2007;463:723–733. doi:10.1098/rspa.2006.1790

24. Lasalle A, Guizard C, Maire E, Adrien J, Deville S. Particles redistribution and structural defect development during ice templating. *Acta Mater.* 2012;60(11):4594–4603. https://doi.org/10.1016/j.actamat.2012.02.023

25. Peppin SSL, Style RW. The physics of frost heave and ice-lens growth. *Vadose Zo J.* 2013;12. doi:10.2136/vzj2012.0049

26. Azmatch TF, Sego DC, Arenson LU, Biggar KW. 2011. Tensile strength and stress–strain behaviour of Devon silt under frozen fringe conditions. *Cold Reg Sci Technol.* 68(1–2):85–90.

27. van Vliet-Lanoë B. 1985. Frost effects in soils. In: Boardman J. ed. *Soils and Quaternary Landscape Evolution*. Chichester, UK: Wiley; 117–158.

28. Carlson LE, Nixon JF. Subsoil investigation of ice lensing at the Calgary, Canada, frost heave test facility. *Can Geotech J.* 1988;25(2):307–319. https://doi.org/10.1139/t88-033

29. Smith SL, Williams PJ. Ice lens orientation around a chilled buried pipe. In: Burgess MM, Harry

DG, Sego DC, eds. Fifth Canadian Permafrost Conference. Centre d'études nordique, Université Laval, Collection Nordicana, No.54;2008: 83–87.

30. Smith SL, Williams PJ. Ice lens formation at a silt–sand interface. *Can Geotech J.* 1995;32(3):488–495. https://doi.org/10.1139/t95-051

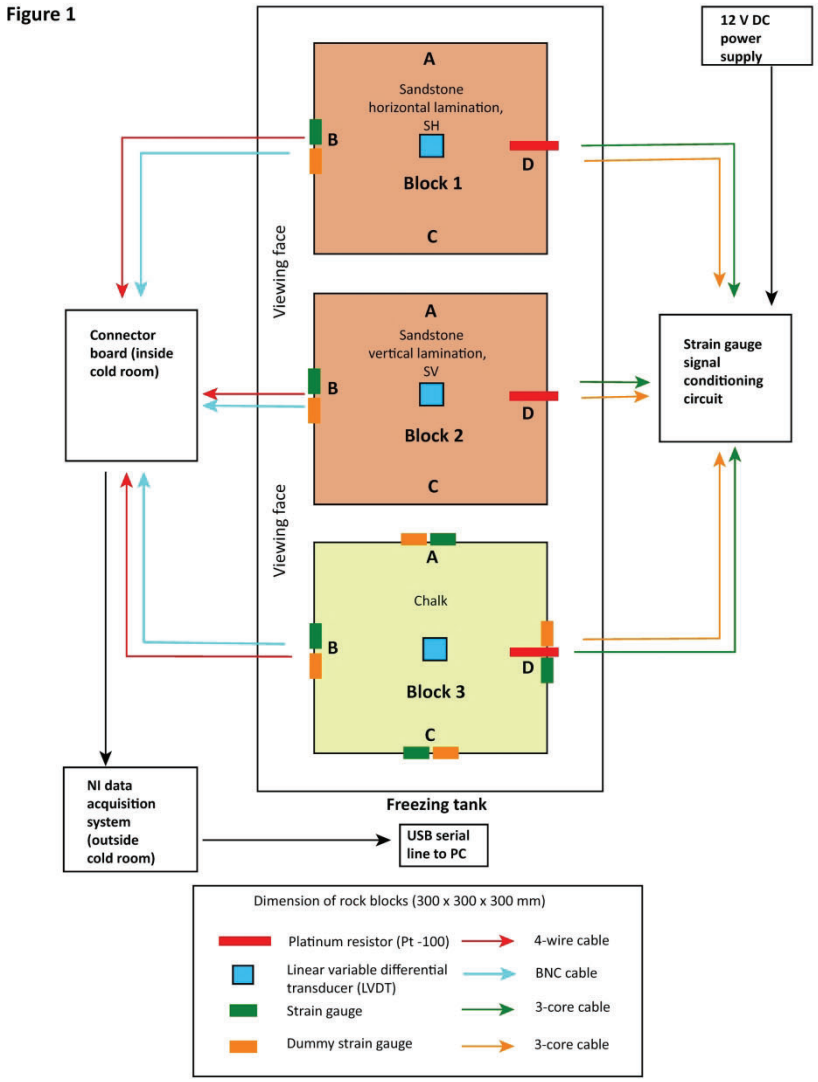


Figure 1. Plan view of the layout of the freezing experiment. 'A', 'B', 'C' and 'D' refer to the vertical faces of the three blocks.

215x279mm (300 x 300 DPI)

Figure 2

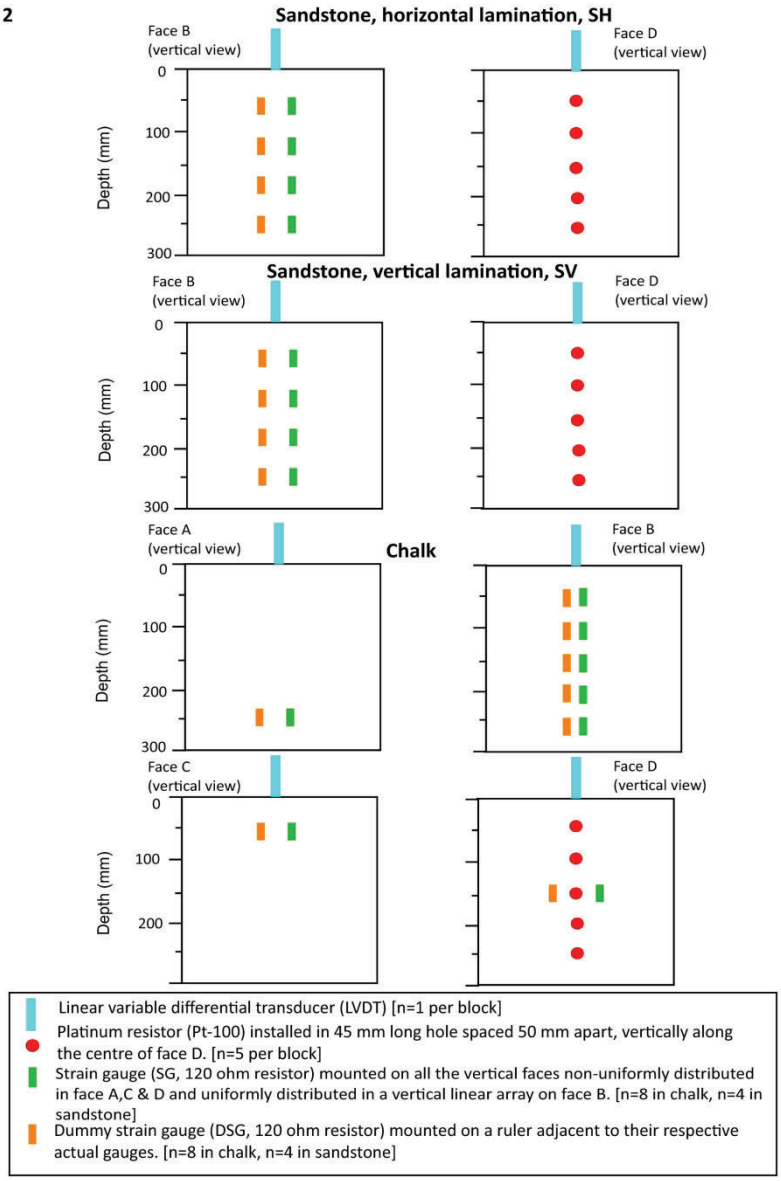


Figure 2. Vertical view of blocks, showing sensor locations.

215x279mm (300 x 300 DPI)

Figure 3

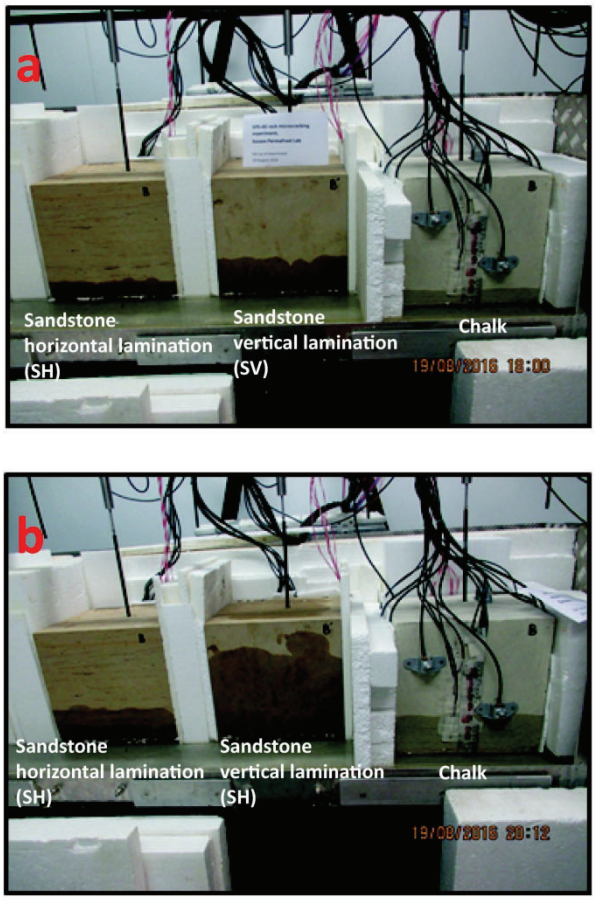


Figure 3. Photographs showing the rising capillary front during (a) early stage of block wetting and (b) two hours later on vertical face B of the three blocks.

215x279mm (300 x 300 DPI)

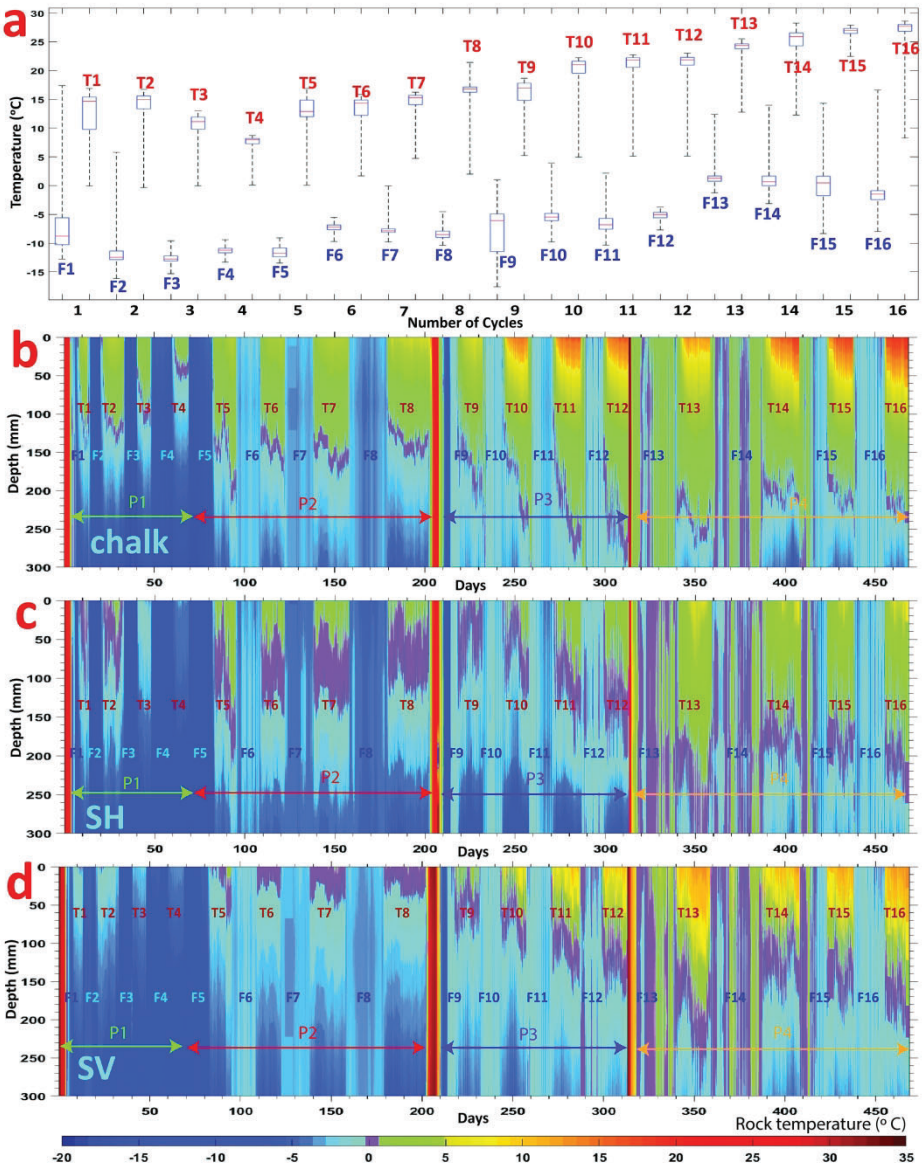


Figure 4. (a) Boxplots of air temperature (±1 std. dev.) during the freezing periods 1–16 (F1–F16) and thawingperiods (T1–T16). Red lines show median values, lower and upper limits of the boxes show lower and upperquartiles, and whiskers extend to maximum and minimum values. Time series of temperature profiles during P1 to P4 (freeze–thaw cycles 1–16) in blocks of (b)chalk, (c) sandstone with lamination horizontally oriented (SH) and (d) sandstone with lamination verticallyoriented (SV).

215x279mm (300 x 300 DPI)

Figure 6

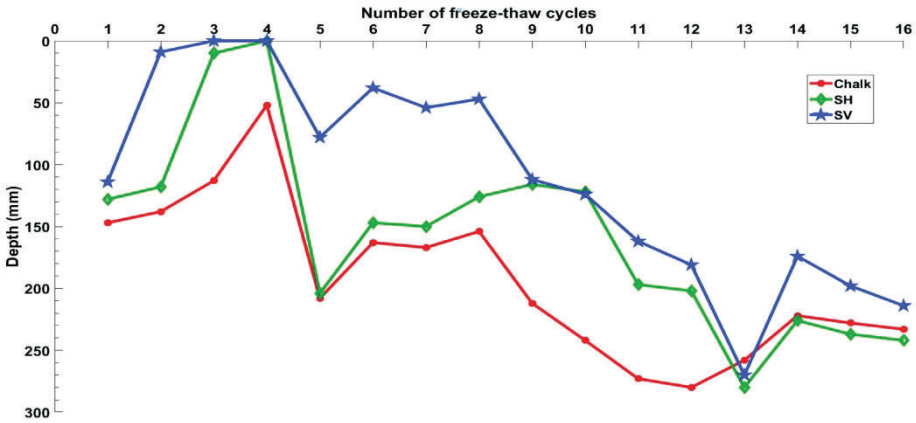


Figure 5. Simulated active-layer thickness during freeze–thaw cycles 1–16.

215x279mm (300 x 300 DPI)

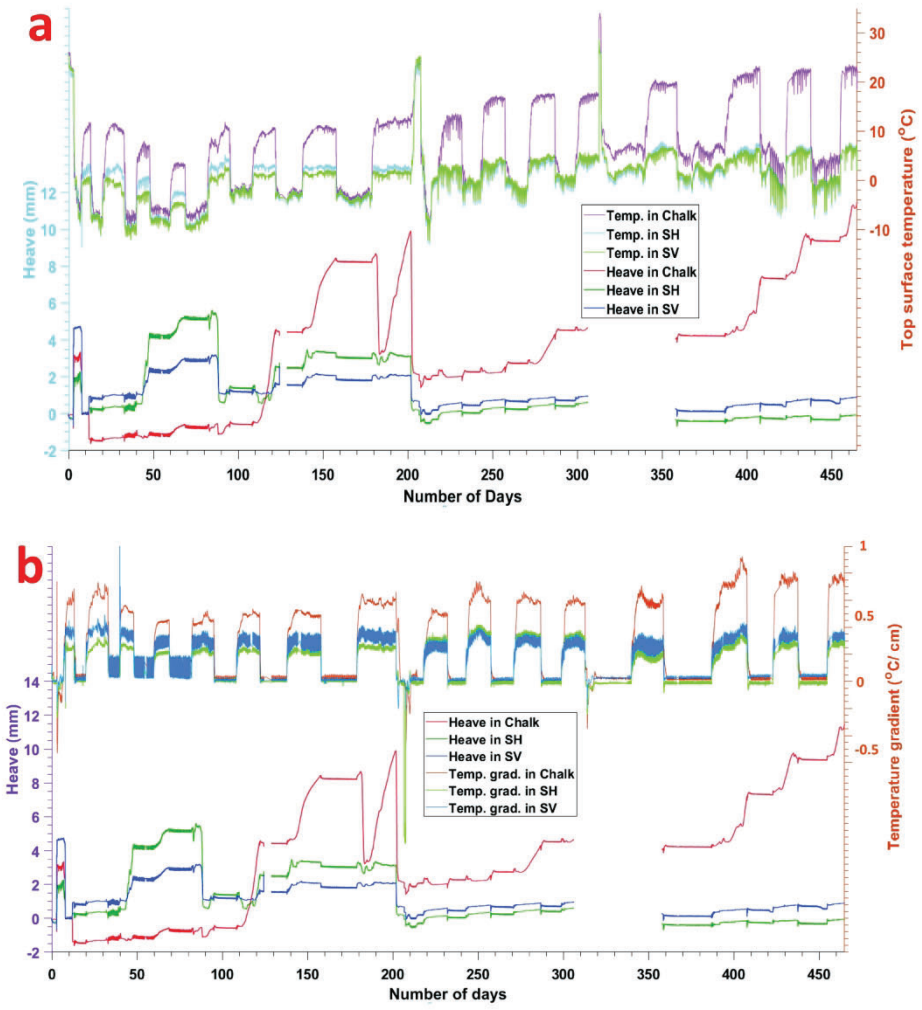


Figure 6. Time series of heave plotted against (a) block-top temperature and (b) temperature gradient for the three blocks during freeze–thaw cycles 1–16. Temperature gradient is averaged over block height (300 mm).

215x279mm (300 x 300 DPI)

Figure 8

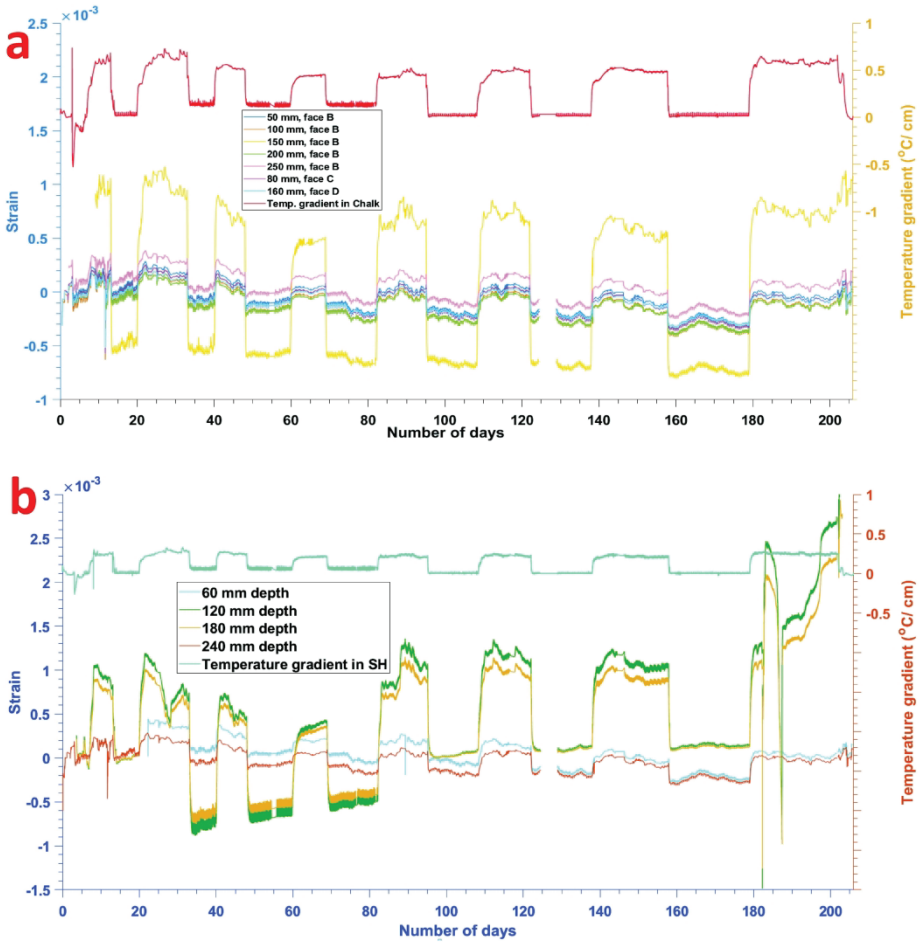


Figure 7. Time series of strain at various depths plotted against temperature gradient during freeze–thaw cycles 1–16 for (a) chalk faces B–D (b) and sandstone with horizontal lamination (SH) face B. Temperature gradient is averaged over block height (300 mm).

215x279mm (300 x 300 DPI)

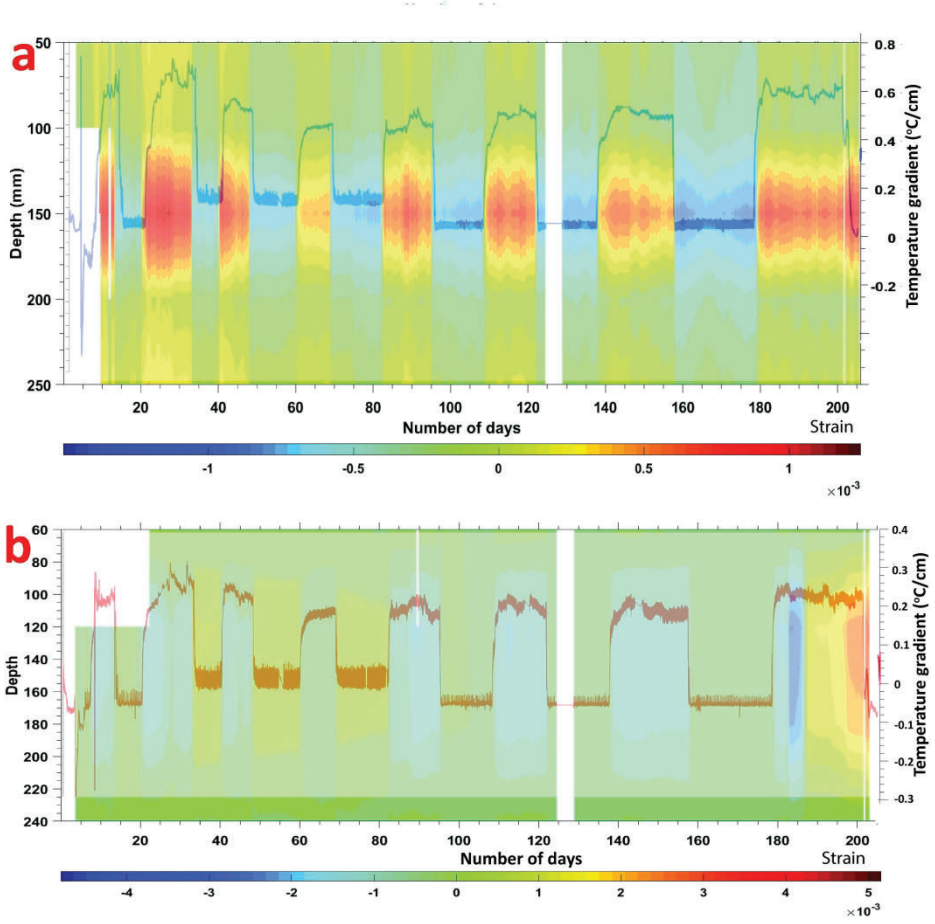


Figure 8. Time series of contoured strain profiles interpolated from measurements at depths of (a) 50, 100, 150, 200 and 250 mm within chalk face B and (b) 60, 120, 180 and 240 mm within SH face B during freeze–thaw cycles 1–16. Strain values are averaged at intermediate depths where no strain data are available. White areas indicate gaps in strain data acquisition.

215x279mm (300 x 300 DPI)

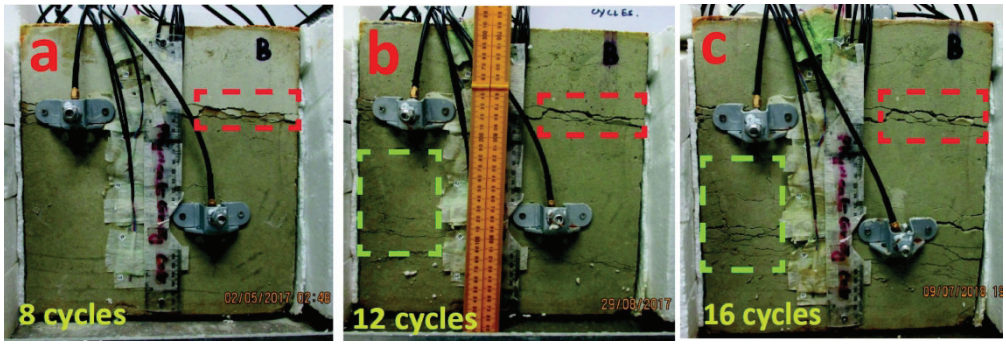


Figure 9. Photographs of macrofacture networks in vertical faces of chalk block after different numbers of freeze–thaw cycles: face B after 8, 12 and 16 cycles (a to c, respectively). Sensors record acoustic emissions and are reported in the companion paper.

194x65mm (300 x 300 DPI)

Figure 11

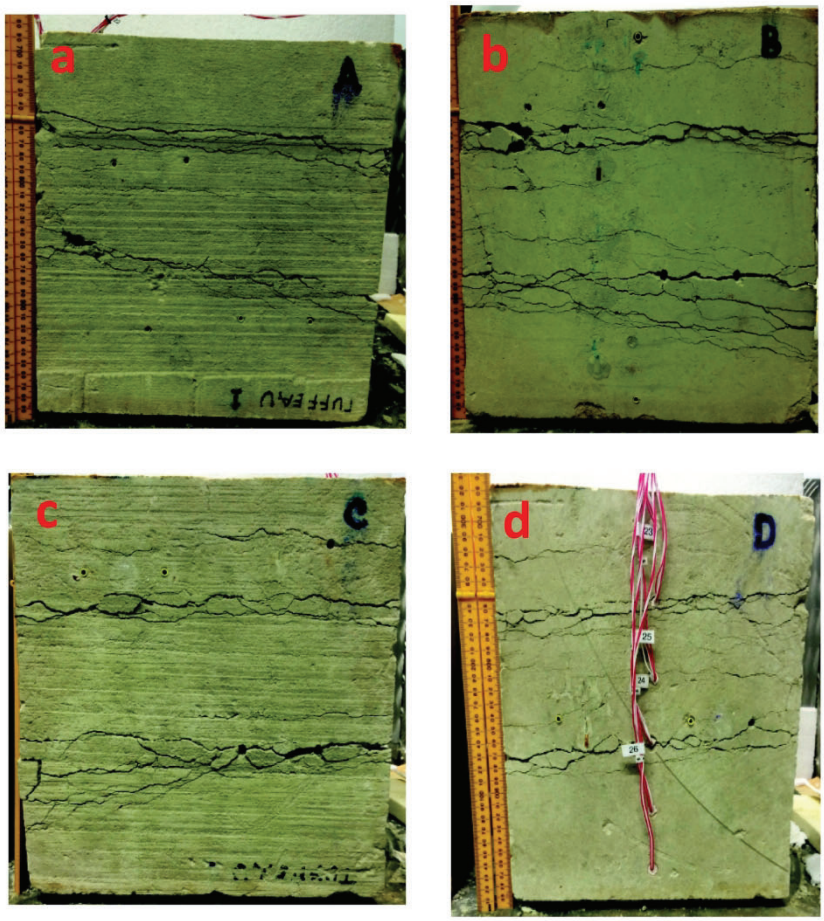


Figure 10. Photographs of macrofacture networks in vertical faces A to D of chalk block (a to d, respectively) and faces B and C of the sandstone horizontal block (e to f) after 16 freeze–thaw cycles. Holes are for installation of sensors within the blocks.

215x279mm (300 x 300 DPI)

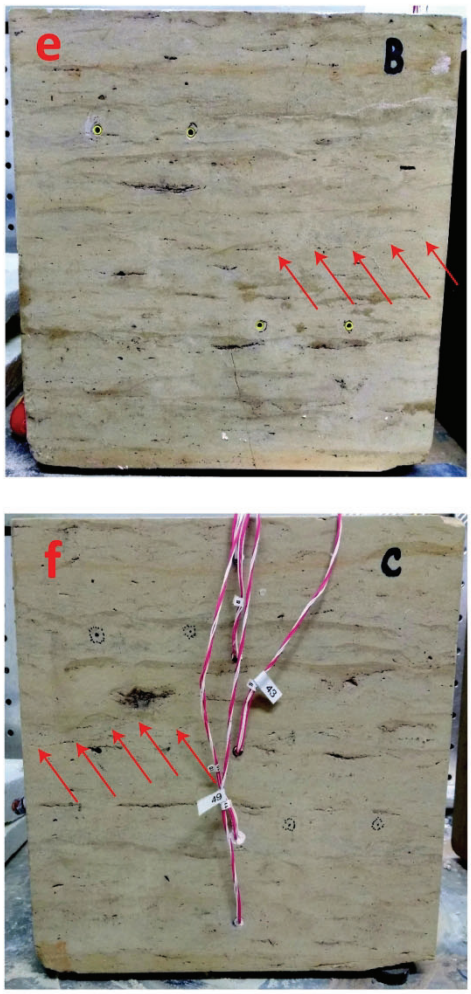


Figure 10. Photographs of macrofacture networks in vertical faces A to D of chalk block (a to d, respectively) and faces B and C of the sandstone horizontal block (e to f) after 16 freeze–thaw cycles. Holes are for installation of sensors within the blocks.

215x279mm (300 x 300 DPI)

Figure 12

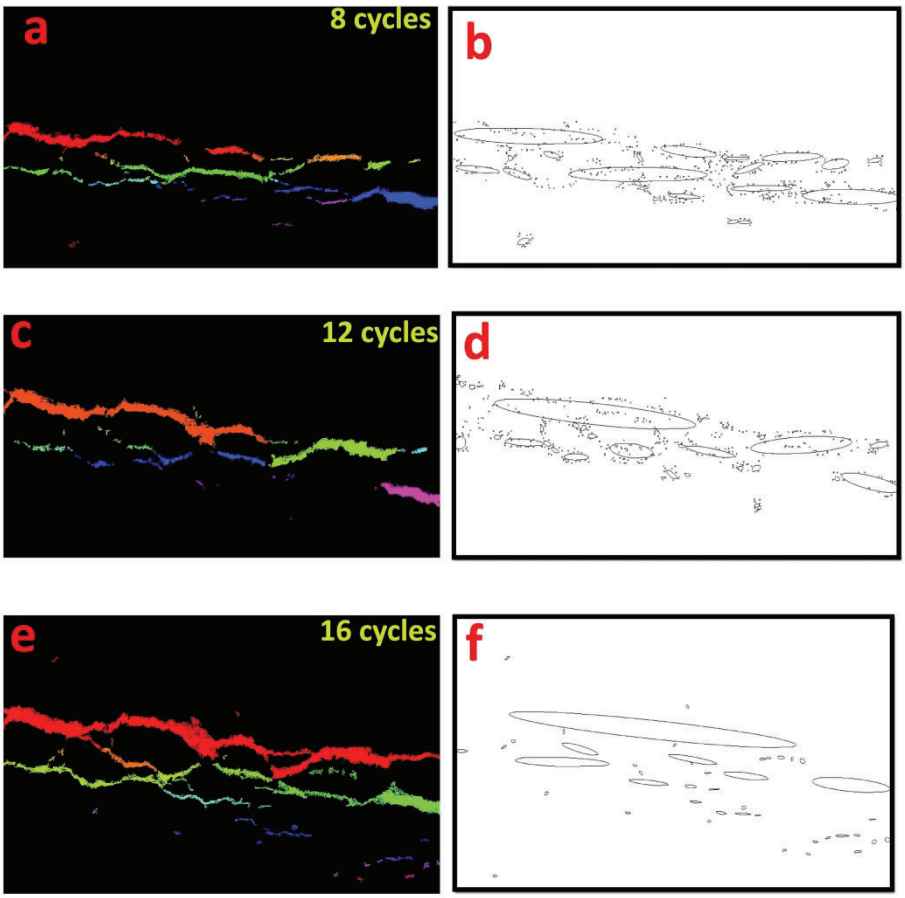


Figure 11. Digital images of macrofracture networks and ellipses fitted around them after freeze–thaw cycles 8 (a and b), 12 (c and d) and 16 (e and f) in the upper part of face B in the chalk block. Location of the diagrams marked by boxes in Fig. 10a-c.

215x279mm (300 x 300 DPI)

Figure 13

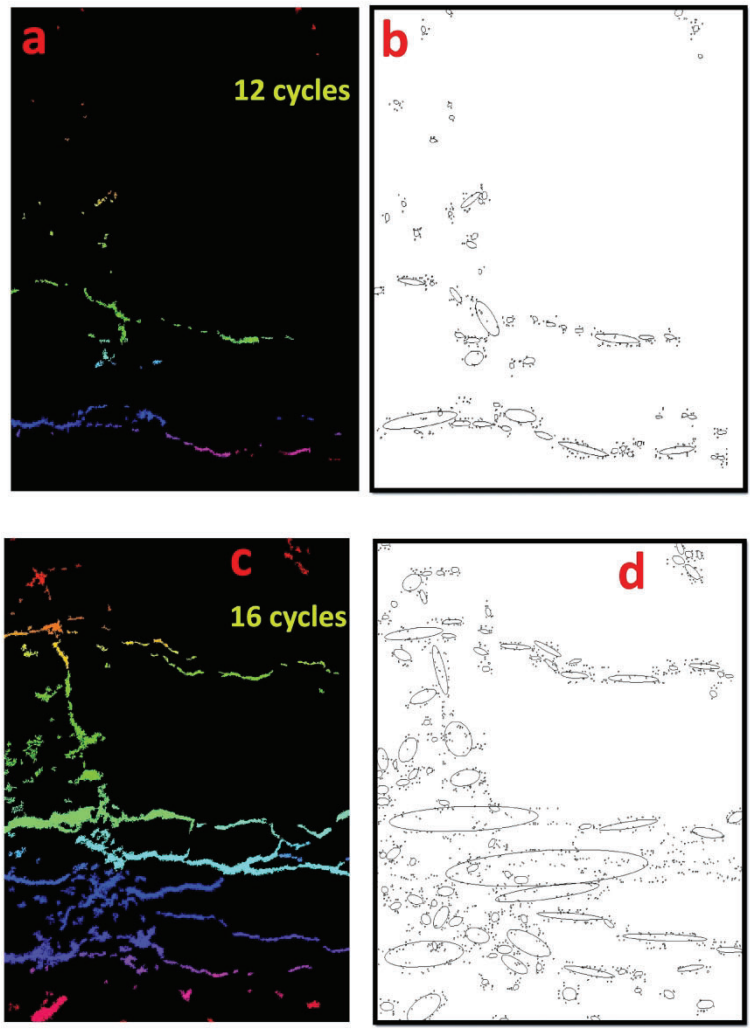


Figure 12. Digital images of macrofracture networks and ellipses fitted around them after freeze–thaw cycles 12 (a and b) and 16 (c and d) in the lower part of face B in the chalk block. Location of the diagrams marked by boxes in Fig. 10b-c.

215x279mm (300 x 300 DPI)

**Figure 14**

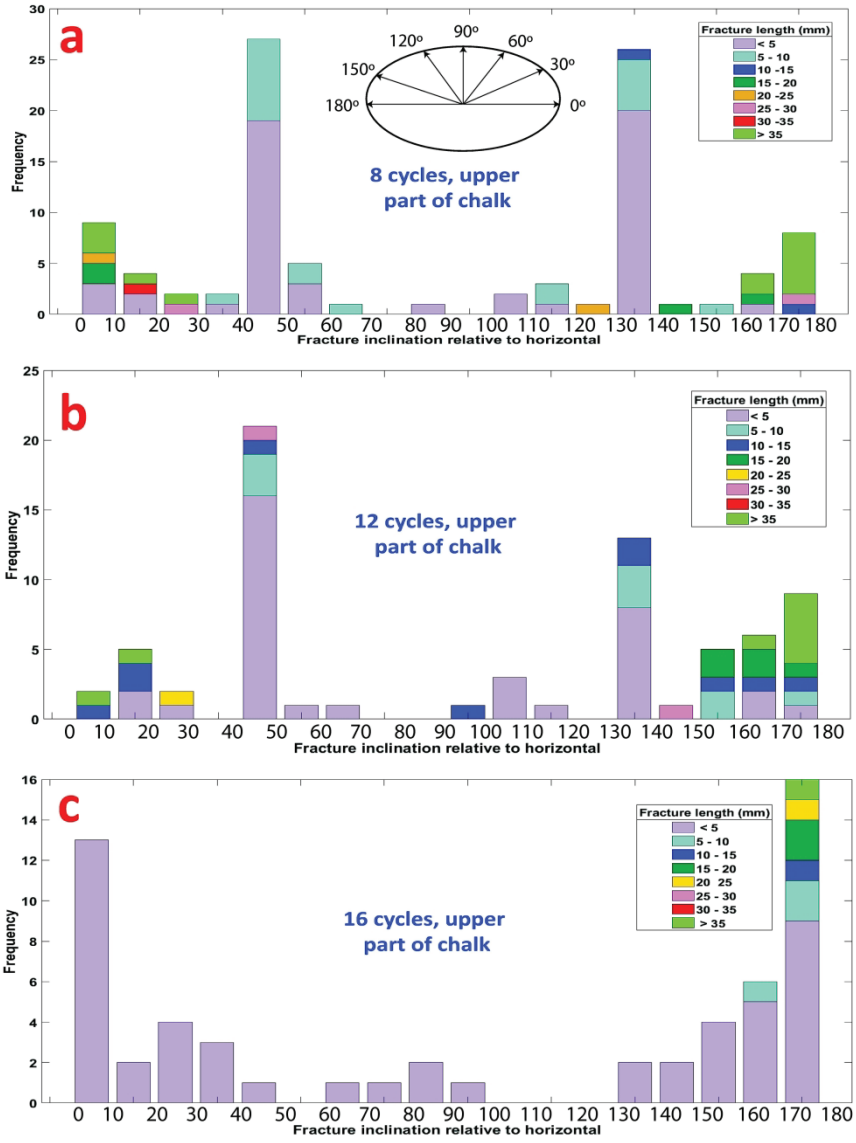


Figure 13. Histograms of fracture inclination and length in the upper fracture network of the chalk block (about 100 mm depth) after 8, 12 and 16 freeze–thaw cycles (a–c, respectively), and in the lower fracture network (about 175–225 mm depth) after 12 and 16 cycles (d and e, respectively). Inset figure in panel a shows orientations of ellipses between 0 and 180°. Note variable scales of the y axes.

215x279mm (300 x 300 DPI)

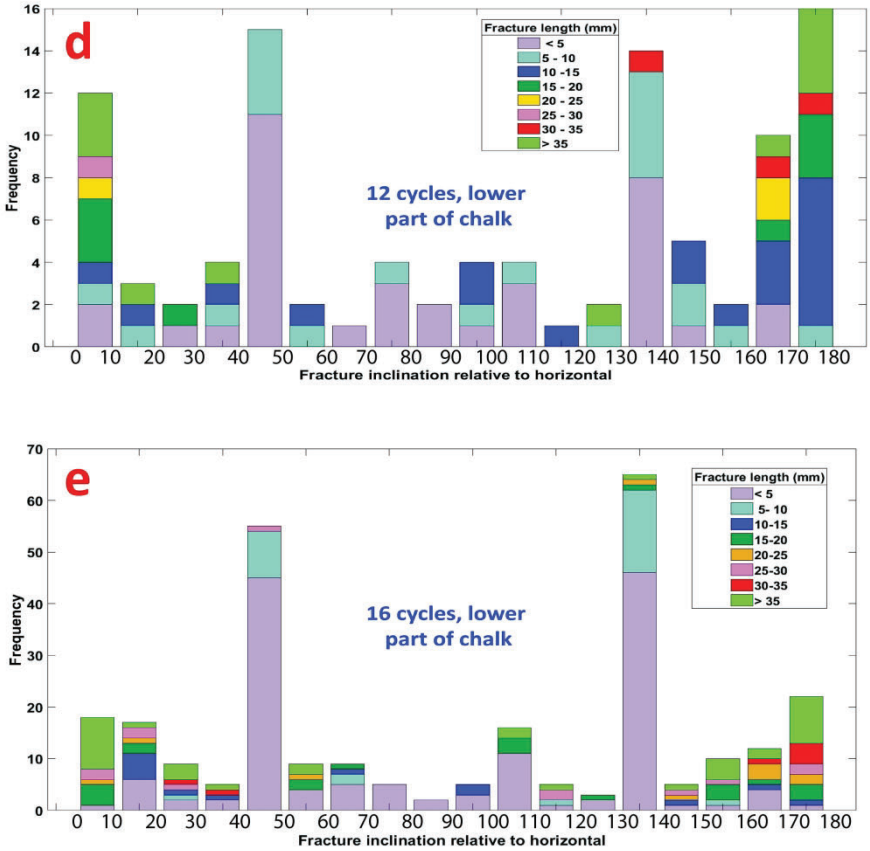


Figure 13. Histograms of fracture inclination and length in the upper fracture network of the chalk block (about 100 mm depth) after 8, 12 and 16 freeze–thaw cycles (a–c, respectively), and in the lower fracture network (about 175–225 mm depth) after 12 and 16 cycles (d and e, respectively). Inset figure in panel a shows orientations of ellipses between 0 and 180°. Note variable scales of the y axes.

215x279mm (300 x 300 DPI)